# Probing Excitons in Transition Metal Dichalcogenides by Drude-Like Exciton Intraband Absorption

# Journal Name

## ARTICLE TYPE

# Probing Excitons in Transition Metal Dichalcogenides by Drude-Like Exciton Intraband Absorption[†]

Siqi Zhao[a], Dawei He[a], Jiaqi He[a], Xinwu Zhang[a], Lixin Yi[a], Yongsheng Wang[*a], and Hui Zhao[*b]

Understanding excitonic dynamics in two-dimensional semiconducting transition metal dichalcogenides is important for developing their optoelectronic applications. Recently, transient absorption techniques based on resonant excitonic absorption have been used to study various aspects of excitonic dynamics in these materials. The transient absorption in such measurements originates from phase-space state filling, bandgap renormalization, or screening effects. Here we report a new method to probe excitonic dynamics based on exciton intraband absorption. In this Drude-like process, probe photons are absorbed by excitons in their intraband excitation to higher energy states, causing a transient absorption signal. Although the magnitude of the transient absorption is lower than the resonant techniques, the new method is less restrictive on the selection of probe wavelength, has a larger linear range, and can provide complementary information on photocarrier dynamics. Using $WS_2$ monolayer and bulk samples as examples, we show that the new method can probe exciton-exciton annihilation at high densities and reveal exciton formation processes. We also found that the exciton intraband absorption cross section of $WS_2$ monolayer is on the order of $10^{-18}$ $cm^2$.

## 1 Introduction

Since the discovery of graphene, interests on two-dimensional (2D) materials have grown rapidly. Transition metal dichalcogenides (TMDs) are among the most extensively studied 2D semiconductors[1]. They have several interesting properties such as transition to a direct bandgap in monolayers (MLs)[2,3], valley-selective optical coupling[4–6], and strong nonlinear optical responses[7–11]. Hence, they are regarded as promising candidates for various electronic and optoelectronic technologies, including field-effect transistors[12,13], integrated circuits[14], solar cells[15], photodetectors[15], and light-emitting diodes[16–18]. Due to their large binding energies, on the order of hundreds of meV[19–22], excitons in 2D TMD are stable at elevated temperatures, and play a key role in determining the optical and electronic properties of these materials. Hence, understanding excitonic dynamics is important for developing applications based on 2D TMDs.

Previously, excitonic dynamics has been studied by various time-resolved techniques, such as transient absorption of visible light, time-resolved photoluminescence[23–26], transient THz conductivity[27–29], dynamical second harmonic generation[30], mid-infrared transient absorption by excitonic internal transitions[31,32], and time-resolved photoemission[33]. Among these techniques, the transient absorption of visible light based on femtosecond lasers is the most widely used method. In such measurements, excitons are either resonantly injected by an ultrashort laser pulse tuned to the optical bandgap of the material or formed from electron-hole pairs injected by a pulse tuned above the quasiparticle bandgap. The dynamics of the excitons is monitored by using a probe pulse with a controlled time delay with respect to the pump pulse, utilizing the transient absorption induced by the excitons. Through such measurements, various aspects of photocarrier and excitonic dynamics in 2D TMDs have been revealed, including thermalization and energy relaxation[34], exciton formation[35], exciton-exciton annihilation[36,37], exciton diffusion[38–47], spin and valley relaxation[48,48–53,53–56], and exciton recombination[25,27,36,41,43,49,53,57–60],

In transient absorption measurements discussed above, the probe pulse is tuned to the exciton resonance, as shown as the blue arrow in Figure 1(a). The transient absorption is induced *via* phase-space state filling, bandgap renormalization, or screen-

ing effects[61]. Although this is a powerful method, transient absorption based on these mechanisms has some limitations. For example, for a given material, the probe photon energy is rather selective, due to the resonant nature of these mechanisms. The dependence of the signal on the exciton density deviates from a linear relation at elevated carrier densities, making interpretation of the results difficult in these regimes.

Here we demonstrate an alternative probe mechanism based on exciton intraband absorption (EIA). Measurements of this type can be performed with any probe photon energy that is smaller than the optical bandgap of the material, and the signal is proportional to the exciton density over a much wider density range. Using $WS_2$ ML and bulk samples as examples, we show that this probe technique can provide complementary information to the resonant-absorption-based techniques.

## 2    Experimental section

The $WS_2$ ML samples were fabricated by mechanical exfoliation onto polydimethylsiloxane (PDMS) substrates. ML flakes were identified by their known optical contrast of about 8% on transparent substrates[62] (Figure S1). Photoluminescence (PL) measurements were performed to further confirm the ML thickness. The PL yield of the region with the smallest optical contrast is orders-of-magnitude higher than other regions, with a narrow peak at 620 nm (Figure S2). A bulk $WS_2$ was exfoliated to another PDMS substrate (Figure S3). Its thickness is about 36 nm, which is estimated from its green light transmission and reflective contrast. Both samples were transferred onto a quartz substrate, and were annealed under $H_2$-Ar mixed gas environment at 200°C for 3 hours.

The transient absorption measurements in transmission geometry were performed with an experimental setup schematically shown in Figure S4. A Ti-doped sapphire laser generates 100-fs pulses with a central wavelength of 820 nm at a repetition rate of about 80 MHz. This output is divided to three parts. One part pumps an optical parametric oscillator, which produces a 620-nm pulse by parametric down conversion. Another part is focused to a beta barium borate (BBO) crystal to produce a 410-nm pulse by second harmonic generation. The last part of the 820-nm pulse is used directly in the measurement.

In this study, the 410-nm pulse was used as the pump pulse to excite the samples. Depending on the experimental configuration, either the 820-nm or the 620-nm pulse was used as the probe pulse. The 410-nm pump pulse was send to a retroreflector on a motorized stage, so that its propagation length (and hence its arrival time at the sample) can be adjusted. The pump and probe pulses were combined by a beamsplitter, and were focused to the sample through a microscope objective lens. The transmitted probe was collimated by another lens, and was detected by a photodiode., which was connected to a lock-in amplifier. A chopper was used in the pump arm to modulate its intensity at about 1 KHz. With this setup, we can measure the differential transmission of the probe, with is defined as $\Delta T/T_0 = (T - T_0)/T_0$, where $T$ and $T_0$ are the transmission coefficients of the sample for the probe with and without the presence of the pump beam, respectively.
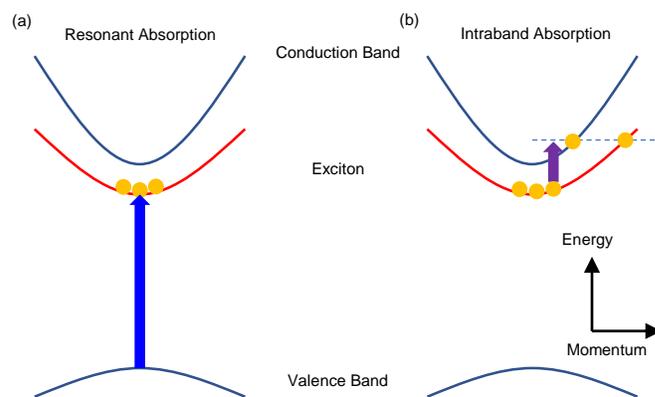


**Fig. 1** Schematics of transient absorption measurements to probe excitons based on resonant absorption (a) and exciton intraband absorption (b).

## 3    Results and discussion

### 3.1   EIA-based transient absorption of monolayer $WS_2$

The EIA-based probe mechanism is schematically shown in Figure 1(b). Here, a probe with a photon energy smaller than the optical bandgap of the material is used. Without an exciton population, the absorption of this probe is achieved by lattice absorption, and is negligibly small. With the presence of excitons, as shown in Figure 1(b), the probe photons can be absorbed by these excitons. In this process, an exciton absorbs one photon [vertical purple arrow in Figure 1(b)]. Since a photon carriers negligibly small momentum, the transition needs to involve phonons to conserve the crystal momentum, as indicated by the dashed line. After the absorption, the exciton can become a free electron-hole pair or a hot exciton. In additional to EIA, the exciton population could also alter the interaction of the probe with the sample *via* other mechanisms, such as screening or biexciton effects. Since the purpose of the probe is to sense the exciton density, the uncertainty of the final states of the excitons after they have been probed is not a concern.

We phenomenologically describe the EIA process. With the presence of excitons, the absorption coefficient of the sample becomes

$$\alpha = \alpha_0 + \Delta\alpha = \alpha_0 + \sigma_{EA} N_{3D}. \qquad (1)$$

$\alpha_0$ denotes the absorption coefficient of the sample without an exciton population. $\sigma_{EA}$ is the cross section of the EIA and $N_{3D}$, the volume exciton density. By using this model, we have assumed that EIA is proportional to the exciton density. This is similar to the linear relation between free-carrier absorption and free-carrier density[46]. According to Beer's Law, the transmission of the sample is related to the absorption coefficient by

$$T = e^{-\alpha L}, \qquad (2)$$

with $L$ being the sample thickness. Hence, the differential transmission

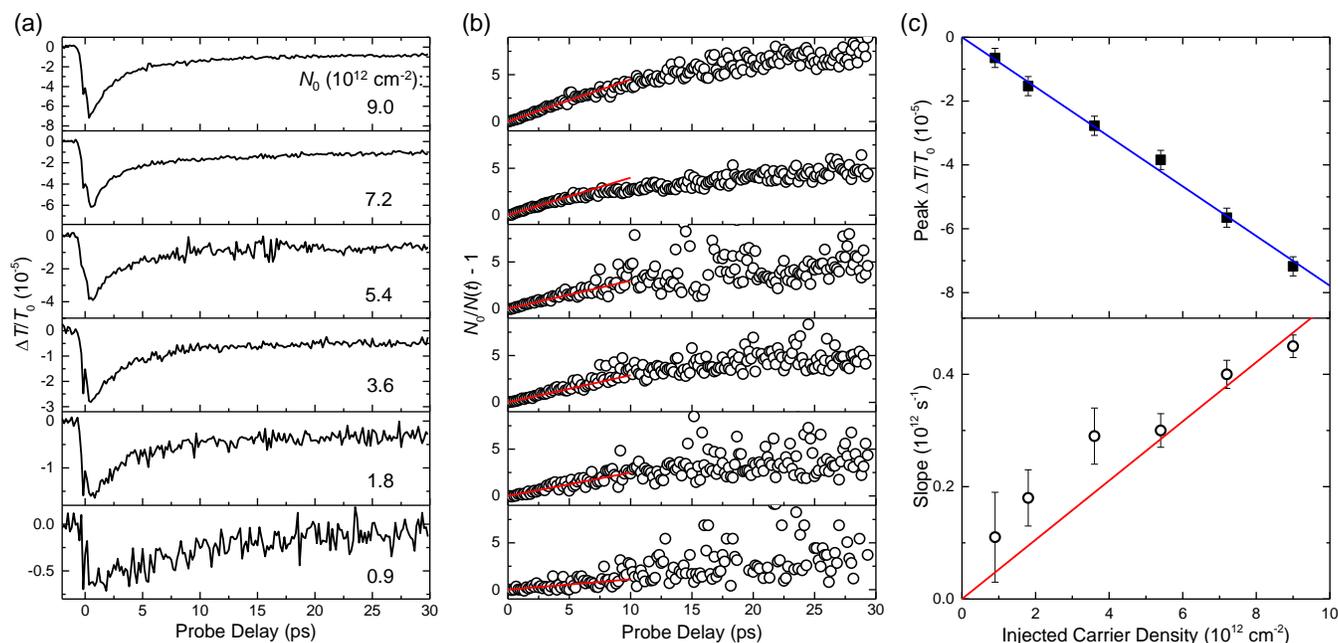$$\Delta T/T_0 = (T - T_0)/T_0 = e^{-\Delta\alpha L} - 1. \qquad (3)$$

**Fig. 2** (a) Differential transmission signal of an 820-nm probe pulse measured from the monolayer WS$_2$ sample with a 410-nm pump pulse. The initially injected carrier density by the pump is labeled in each panel. (b) The quantity $N_0/N(t) - 1$ calculated from the data shown in (a). The red lines are linear fits. (c) The peak differential transmission signal (top) and the slope of the linear fit (bottom) as a function of the injected carrier density.

Under the condition of $\Delta\alpha L \ll 1$, we have

$$\Delta T/T_0 \approx -\Delta\alpha L = -\sigma_{EA}N_{3D}L = -\sigma_{EA}N, \quad (4)$$

where $N$ is the areal exciton density.

The top panel of Figure 2(a) shows the differential transmission signal of an 820-nm probe pulse measured from the WS$_2$ ML sample with a 410-nm and 90 $\mu$J cm$^{-2}$ pump pulse. Using an absorption coefficient [63] of $7 \times 10^7$ m$^{-1}$, we estimate that the pump injects a peak carrier density of about $N_0 = 9.0 \times 10^{12}$ cm$^{-2}$ at the center of the pump laser spot [64]. It has been shown that in TMD MLs, the excitons are formed from free electron-hole pairs on a picosecond time scale [35,65,66], and are stable at room temperature due to their large binding energies [21,22,63,67–70]. Hence, the observed signal is mainly induced by the excitons. Since the probe photon energy (1.51 eV) is far below the optical bandgap of WS$_2$ ML (2.00 eV), the transient absorption is expected to be induced by EIA. The negative sign of the differential transmission signal indicates that the excitons induce a decrease of the probe transmission, and hence an increase of the absorption. This is opposite to the phase-space state filling mechanism, but is consistent with the EIA mechanism. When the pump fluence is reduces, and therefore the injected carrier density is lowered proportionally, the magnitude of the signal decreases, as shown in the other panels of Figure 2(a). The upper panel of Figure 2(c) shows the peak signal as a function of the injected carrier density. The magnitude of the signal is proportional to the carrier density, as confirmed by a linear fit (the blue line). This reflects the fact that the EIA coefficient is proportional to the exciton density without any saturation effect even at such high exciton densities. From the slope,

we deduce a cross section $\sigma_{EA} \approx 8 \times 10^{-18}$ cm$^2$. This value is in the same order of magnitude with free carrier absorption cross sections of traditional 3D semiconductors like silicon [46] and ML MoS$_2$ [71].

### 3.2 Exciton-exciton annihilation at high densities

From Figure 2(a), the decay of the signal is slower at lower densities. Such a density-dependent exciton recombination process indicates that the dynamics is not governed by a single-molecular process. Indeed, our attempts confirmed that the decay of the signal cannot be fit by a single-exponential function. This is, however, expected since at such high densities, exciton-exciton annihilation is known to dominate the exciton dynamics [25,31,36,37]. With the contribution of exciton-exciton annihilation, the decay of the exciton density can be written as

$$\frac{dN}{dt} = -\frac{1}{\tau}N - \frac{1}{2}\gamma N^2, \quad (5)$$

where $\tau$ and $\gamma$ are the density-independent exciton lifetime and exciton-exciton annihilation rate, respectively. When $t \ll \tau$, we can ignore the contribution of the first term on the right-hand side and find

$$\frac{N_0}{N(t)} - 1 = \gamma N_0 t, \quad (6)$$

where $N_0$ is the initial exciton density [36]. Figure 2(b) shows the quantity $[N_0/N(t)] - 1$, which is calculated from the data shown in Figure 2(a), as a function of the probe delay. The initial part can be described by the exciton annihilation model (red lines). The deviation from the linear relation at later probe delays can
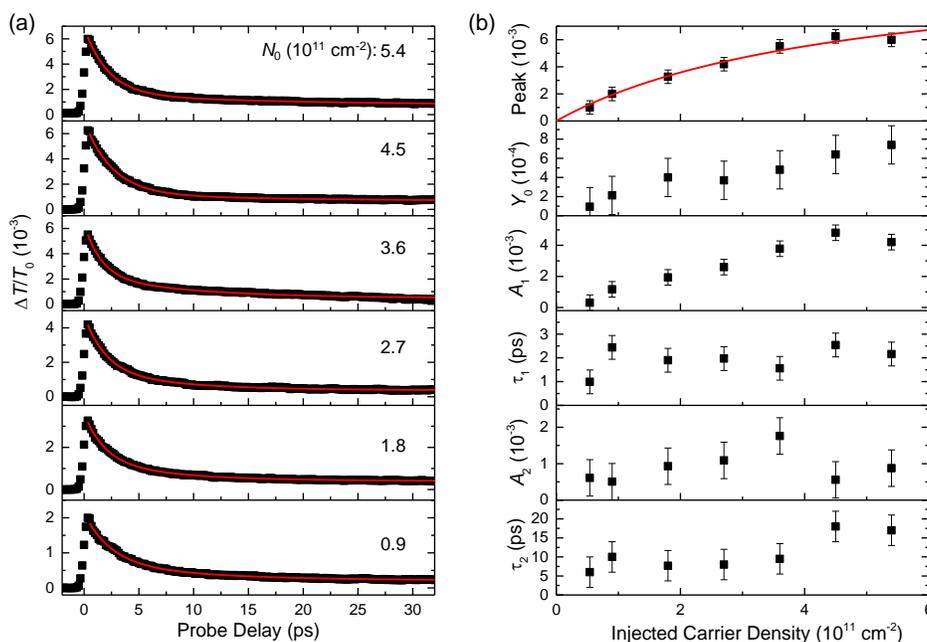
**Fig. 3** (a) Differential transmission signal of a 620-nm probe pulse measured from the WS$_2$ ML sample with a 410-nm pump pulse. The initially injected carrier density by the pump is labeled in each panel. (b) The peak differential transmission signal (top panel) and fitting parameters (other panels) as a function of the injected carrier density.

be attributed to the contribution from the first item in Eq. 5. Furthermore, the slopes of the linear fits shown in Figure 2(b) are plotted in the lower part of Figure 2(c). Despite of the relatively large uncertainties due to the low signal level, the result shows a linear dependence as expected from Eq. 6. A linear fit (red line) gives an annihilation rate of about 0.05 cm$^2$ s$^{-1}$. This result is within one order of magnitude with previously reported values of [37] 0.043 cm$^2$/s in MoS$_2$, 0.33 cm$^2$/s in MoSe$_2$ [36], 0.41 cm$^2$/s in WS$_2$ [25], and 0.13 cm$^2$/s in WSe$_2$ [31]. We note that the annihilation rate measured here is at higher carrier densities than previous studies regimes [25,31,36,37], thanks to the linear relation bewteen the signal and the exciton density at such high densities.

### 3.3 Comparison of EIA and resonant transient absorption measurements

For comparison, we also performed differential transmission measurements with a 620-nm probe. Tuning to the optical bandgap (the A-exciton resonance) of WS$_2$ ML, the probe senses the pump-injected photocarriers and excitons by the phase-space state filling, bandgap renormalization, or screening effects [61]. Figure 3(a) shows the results with different values of the injected carrier density. Note that the densities used in these measurements are much lower than the 820-nm probe measurements. The peak differential transmission signal is plotted in the top panel of Figure 3(b) as a function of the carrier density. Unlike the 820-nm probe, here the signal is not a linear function of the density. Instead, the signal saturates at higher densities.

In the saturated absorption regime, the absorption coefficient of a sample depends on the incident light intensity, which takes the form of $\alpha(I) = \alpha_0/(1 + I/I_{sat})$, where $\alpha_0$ is the linear absorption coefficient and $I_{sat}$, the saturation intensity [72]. In general,

such saturation occurs when a significant fraction of the available electrons (states) are excited (filled) by the excitation. We note that in these measurements, the pump absorption is not expected to saturate because of the low fluences used: The peak fluence is about 5 $\mu$J cm$^{-2}$, injecting a carrier density that is below 10$^{12}$ cm$^{-2}$. It has been reported [73] that for 532-nm and 6-ns pulses, the saturation occurs at a fluence higher than 1 J cm$^{-2}$. For 200-fs pulses used here, the extrapolated saturation fluence is on the order of 300 $\mu$J cm$^{-2}$. One expects the saturation fluence for the 410-nm pump used here to be similar to or even higher than (due to the larger densities of states) the 532-nm pulse. Indeed, the linear power dependence of the EIA-based signal (Figure 2) for a pump fluence up to 100 $\mu$J cm$^{-2}$ further confirms this argument. Therefore, the saturation effect can be attributed to the saturation of the probe absorption by the excitons injected by the pump pulse. This effect can be described as $\Delta\alpha/\alpha_0 = (\alpha - \alpha_0)/\alpha_0 \propto 1/(1 + N/N_{sat})$, where $N_{sat}$ is as the saturation density. By fitting the data with this model, we found a saturation density of about 4.7 $\times 10^{11}$ cm$^{-2}$. Such a saturation effect of the resonant pump-probe measurement is well known, and hinders accurate measurement of the excitonic dynamics in high-density regimes.

The decay of the signal shown in Figure 3(a) was fit by a double exponential function, $\Delta T/T_0 = Y_0 + A_1\exp(-t/\tau_1) + A_2\exp(-t/\tau_2)$. The results are shown as the red curves in Figure 3(a), with the fitting parameters summarized in Figure 3(b). The background, $Y_0$, increases with the injected density and is about 10 % of the peak signal. The parameters $A_1$ and $A_2$ represents the magnitudes of the fast and slow decay processes, respectively. Both of them increase with the injected carrier density for low densities, and saturate at higher densities. The large uncertainties of the data
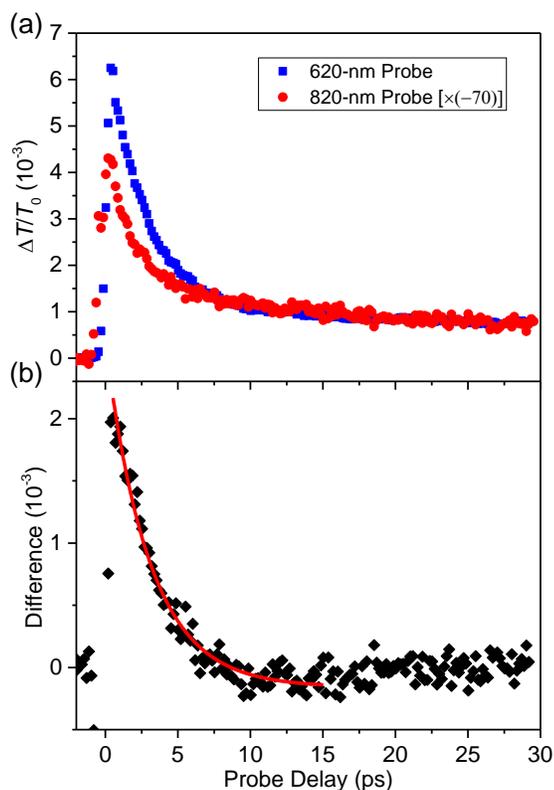
**Fig. 4** (a) Differential transmission signal measured with 620-nm (blue squares) and 820-nm probes (red circles), respectively. The injected densities are $7.2 \times 10^{12}$ for 820-nm and $5.4 \times 10^{11}$ for 620-nm probes. The 820-nm signal was scaled so that the two match at late probe delays. (b) The differential between the two signals shown in (a). The red curve is a single-exponential fit with a decay time of $3.0 \pm 0.3$ ps.

in the initial phase of the photocarrier dynamics. More recently, it has been shown that the fast-decay component in the resonant transient absorption measurement is sensitive to the initial conditions of the photocarriers: It only exists when free-carriers are injected, and is absent when excitons are resonantly injected. Based on this feature, the fast-decay process was attributed to the formation of excitons from free-carriers[35]. This conclusion is consistent with the well-established fact that free carriers are more efficient in producing transient absorption at exciton resonance than excitons[61]. The time scale of exciton formation deduced, on the order of several picoseconds, is also consistent with both results obtained from a different technique[66] and theory[65]. Hence, the EIA-based measurement provides further confirmation of this assignment. This illustrates that the transient absorption techniques with the two mechanisms can provide complementary information to reveal photocarrier dynamics in TMDs. The absence of a fast-changing component in EIA based measurement during the exciton formation process further confirms that the cross sections of EIA and of the free carrier absorption are comparable. As such, the peak signal plotted in Figure 2(c) has contributions from both excitons and free carriers and, strictly speaking, the absorption cross section deduced from the linear fit in Figure 2(c) is a mixture of both. One could use signals at a later delay (after exciton formation is complete) to extract a cross section only for EIA; However, the result would be influenced by the density-dependent exciton recombination. Nevertheless, for an order-of-magnitude estimation, either method is sufficient.

### 3.4 EIA-based and resonant transient absorption of bulk WS$_2$

We studied a bulk WS$_2$ flake with a thickness of about 36 nm. The top panel of Figure 5(a) shows the differential transmission signal of the 820-nm probe with a 410-nm pump fluence of 90 $\mu$J cm$^{-2}$. Due to strong absorption of the pump, the excited areal carrier density *per layer* decreases as the pump propagates into the sample, from about $9 \times 10^{12}$ in the first layer to about $1 \times 10^{12}$ cm$^{-2}$ in the last layer. The corresponding areal carrier density of the whole film is about $1.6 \times 10^{14}$ cm$^{-2}$. The other panels of Figure 5(a) are results obtained with different injected densities, as labeled. Similar to ML, the peak signal is proportional to the injected density, as plotted in upper panel of Figure 5(c). The linear fit (blue line) gives a cross section $\sigma_{EA}$ of about $1.3 \times 10^{-18}$ cm$^2$. This value is about 5 times smaller than obtained from the ML sample. It is possible that different bandstructures and exciton binding energies are responsible for the difference.

Besides the apparent oscillating component, which will be discussed later, the signal decays faster with increasing the injected density. Using the same exciton-exciton annihilation model, Figure 5(b) shows the linear increase of $N_0/N(t) - 1$ with time. The data is consistent with this model. The slope of the fits shown in Figure 5(b) are summarized in the lower panel of Figure 5(c). Except the two low-density points, the result is reasonably consistent with the annihilation model. No effort was attempted to extract an annihilation rate, since in bulk, the exciton density is different from layer to layer, and the signal is the summer of the
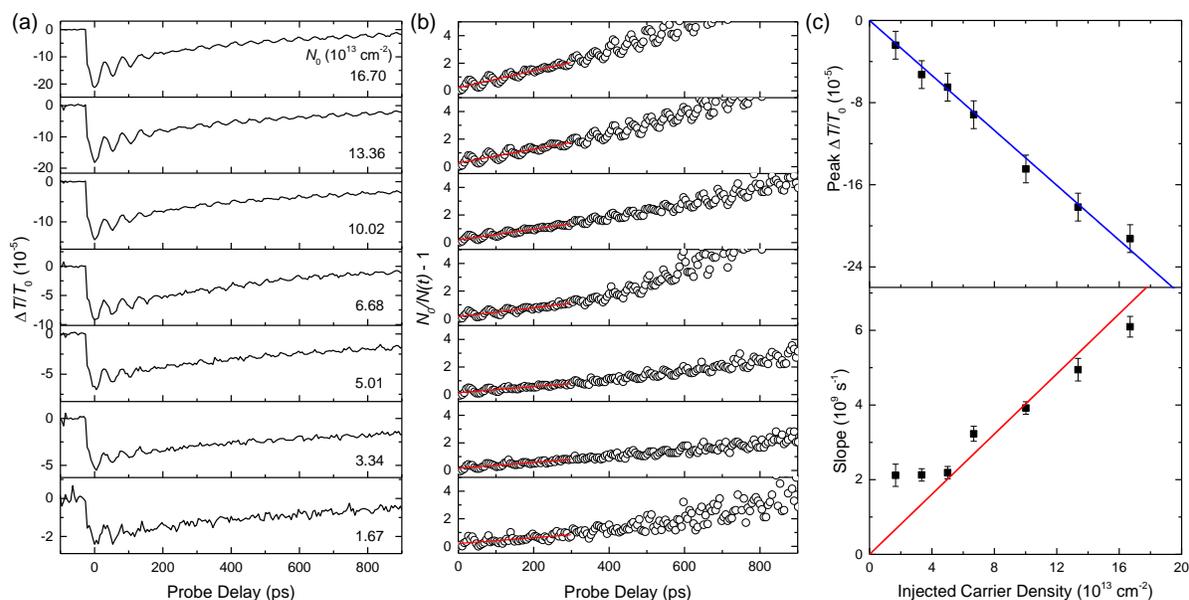
prevent a more detailed analysis on their density dependence. The slow time constant ($\tau_2$) of about 10 ps can be attributed to the exciton lifetime. However, we note that such analysis is less reliable at higher densities, since the signal is no longer proportional to the exciton density. The fast time constant ($\tau_1$) of about 2 ps shows no apparent density dependence. This component is absent with the 820-nm probe. This suggests that the EIA-based transient absorption measurements can provide complementary information on photocarrier dynamics to resonant-absorption based measurements. Figure 4(a) shows a direct comparison of the two measurements. The signal of the 820-nm probe is multiplied by a factor of -70, so that at later probe delays the two curves overlap. Apparently, the signal from the 620-nm probe has an additional component at early delays. The difference of the two curves is shown in Figure 4(b), which can be fit by a single-exponential function with a time constant of about 3 ps (red curve).

In previous transient absorption measurements of TMDs based on resonant absorption, a fast-decay component (picosecond time scale) has been generally observed[49,57]. This phenomenon could be attributed to rapid loss of carriers to defect states. However, if that was the case, the fast-decay component should also be observed in the EIA-based probe, since losing carriers is expected to cause a decrease of the signal, too. The absence of the fast-decay component suggests that there is no rapid loss of carrier density

**Fig. 5** (a) Differential transmission signal of an 820-nm probe pulse measured from a bulk WS$_2$ sample with a 410-nm pump pulse. The initially injected areal carrier density by the pump is labeled in each panel. (b) The quantity $N_0/N(t) - 1$ calculated from the data shown in (a). The red lines are linear fits. (c) The peak differential transmission signal (top) and the slope of the linear fit (bottom) as a function of the injected carrier density.

effects in individual layers.

In Figure 6, the oscillating component of the signal is separated from the slow-varying part. This was done by fitting the data with an exponential function, as indicated by the red curve in Figure 6(a). The oscillating component is then obtained by subtracting this slow-varying component from the data, as shown in Figure 6(b). By fitting the data with a sinusoidal function with an exponentially decaying amplitude, we found a period of about 50 ps. Previously, oscillatory differential reflection signal has been reported from MoS$_2$ multilayer samples, with period of the same order of magnitude [74], and was attributed to coherent lattice vibration. We expect the oscillatory signals observed here are of a similar origin. However, we are unable to attribute this oscillation to any known phonon modes of WS$_2$, since it corresponds to a very low-energy process.

Finally, we performed resonant transient absorption measurements with a 620-nm probe, to compare with the EIA-based measurement. Figure 7(a) shows the obtained differential transmission signal at various injected carrier densities. The decay of the signal is fit by an exponential function, $\Delta T/T_0 = A\exp(-t/\tau) + Y_0$, as shown as the red curves. The fitting parameters obtained are plotted in Figure 7(b). As in ML, the peak signal is a nonlinear function of the carrier density, as indicated by the fit of the saturation model (red line). The decay time constant is about several hundred picoseconds to 1 ns, indicating the long lifetime of excitons in bulk WS$_2$. We note that the oscillatory component of the signal was not observed here, because the carrier-induced signal is much stronger due to the resonant nature of the probe.

## 4   Conclusion

We have demonstrated a new method to probe excitonic dynamics in TMD monolayer and bulk samples based on exciton in-
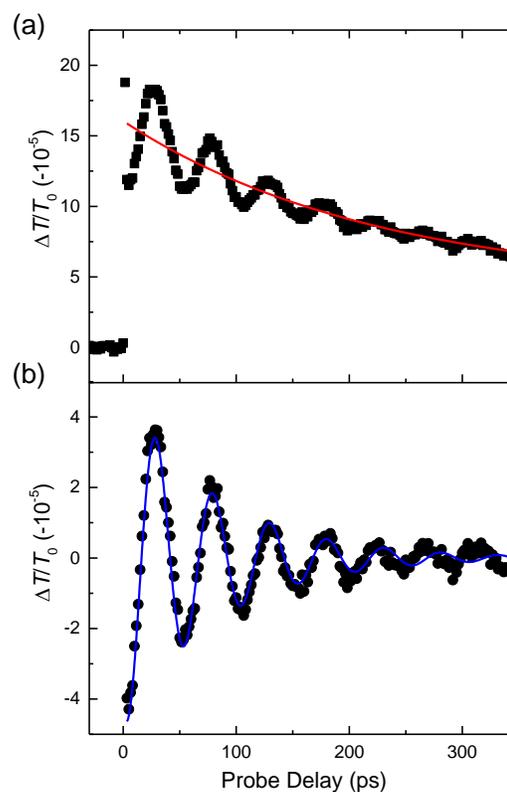


**Fig. 6** (a) Differential transmission signal measured with 820-nm probe. The red curve is an exponential fit. (b) The oscillatory component of the data shown in (a) obtained by subtracting the slow-vary component (red curve) from the data. The oscillatory data was fit by a sinusoidal function with a period of about 50 ps (blue curve).
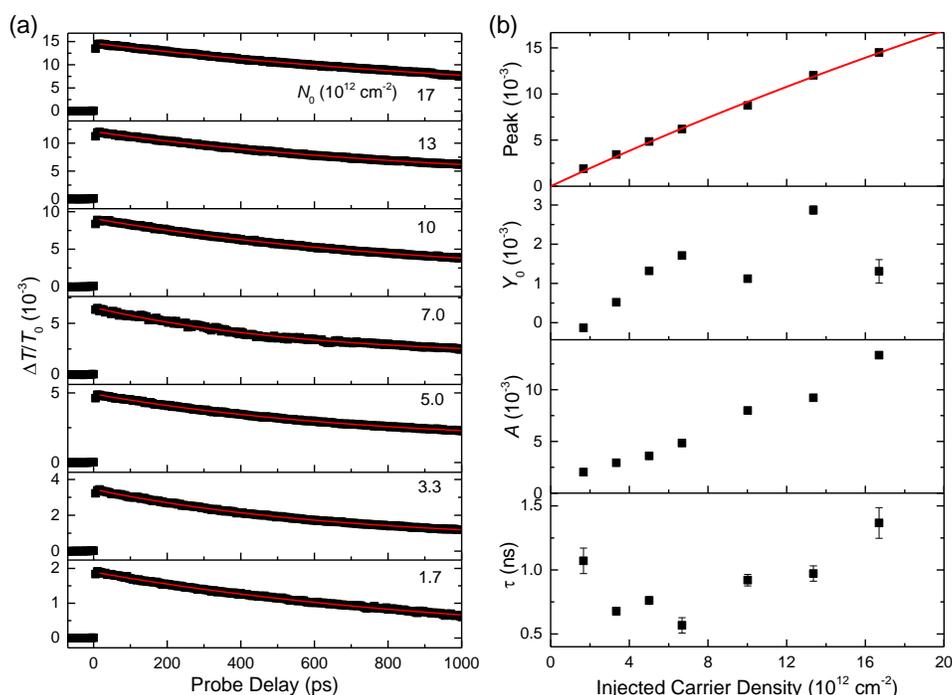
**Fig. 7** (a) Differential transmission signal of a 620-nm probe pulse measured from the bulk $WS_2$ sample with a 410-nm pump pulse. The initially injected carrier density by the pump is labeled in each panel. (b) The peak differential transmission signal (top panel) and fitting parameters (other panels) as a function of the injected carrier density.

traband absorption. Compared to resonant transient absorption techniques, the magnitude of the signal is about three orders of magnitude lower. However, several advantages make it attractive as an alternative technique. First, this approach is less restrictive on the selection of the probe wavelength. Unlike resonant techniques that require the probe to be near the optical bandgap of the sample, the EIA-based measurement can be performed with any probe with a photon energy smaller than the optical bandgap. Second, the EIA-based transient absorption signal is proportional to the carrier density even at a level of $10^{13}$ cm$^{-2}$, which is much higher than the saturation density of the resonant techniques. Taking advantage of the extended linear range, we studied exciton-exciton annihilation in $WS_2$ ML at higher densities than previously reached. Third, we found that, unlike the resonant techniques, the EIA-based transient absorption technique is similarly sensitive to free electron-hole pairs and excitons, which allowed us to obtain further confirmation of the exciton formation process. The EIA-based method is also different from the transient absorption technique based on dipole-allowed $1s$-$2p$ transitions of excitons [31,32]. Although this powerful method can distinguish different types of excitons and allow access to important information such as excitonic internal energy levels, oscillator strengths, and many-body interactions parameters, it requires mid-infrared probes that are resonant to such transitions.

## Acknowledgment

## References

1 Z. Lin, A. McCreary, N. Briggs, S. Subramanian, K. H. Zhang, Y. F. Sun, X. F. Li, N. J. Borys, H. T. Yuan, S. K. Fullerton-Shirey, A. Chernikov, H. Zhao, S. McDonnell, A. M. Lindenberg, K. Xiao, B. J. LeRoy, M. Drndic, J. C. M. Hwang, J. Park, M. Chhowalla, R. E. Schaak, A. Javey, M. C. Hersam, J. Robinson and M. Terrones, *2D Mater.*, 2016, **3**, 042001.

2 K. F. Mak, C. Lee, J. Hone, J. Shan and T. F. Heinz, *Phys. Rev. Lett.*, 2010, **105**, 136805.

3 A. Splendiani, L. Sun, Y. Zhang, T. Li, J. Kim, C. Y. Chim, G. Galli and F. Wang, *Nano Lett.*, 2010, **10**, 1271–1275.

4 D. Xiao, G. B. Liu, W. Feng, X. Xu and W. Yao, *Phys. Rev. Lett.*, 2012, **108**, 196802.

5 H. Zeng, J. Dai, W. Yao, D. Xiao and X. Cui, *Nat. Nanotechnol.*, 2012, **7**, 490–493.

6 K. F. Mak, K. He, J. Shan and T. F. Heinz, *Nat. Nanotechnol.*, 2012, **7**, 494–498.

7 H. Zeng, G.-B. Liu, J. Dai, Y. Yan, B. Zhu, R. He, L. Xie, S. Xu, X. Chen, W. Yao and X. Cui, *Sci. Rep.*, 2013, **3**, 1608.

8 N. Kumar, S. Najmaei, Q. Cui, F. Ceballos, P. M. Ajayan, J. Lou

and H. Zhao, *Phys. Rev. B*, 2013, **87**, 161403.

9 L. M. Malard, T. V. Alencar, A. P. M. Barboza, K. F. Mak and A. M. de Paula, *Phys. Rev. B*, 2013, **87**, 201401.

10 Y. Li, Y. Rao, K. F. Mak, Y. You, S. Wang, C. R. Dean and T. F. Heinz, *Nano Lett.*, 2013, **13**, 3329–3333.

11 X. Yin, Z. Ye, D. A. Chenet, Y. Ye, K. O'Brien, J. C. Hone and X. Zhang, *Science*, 2014, **344**, 488–490.

12 B. Radisavljevic, A. Radenovic, J. Brivio, V. Giacometti and A. Kis, *Nat. Nanotechnol.*, 2011, **6**, 147–150.

13 B. Radisavljevic and A. Kis, *Nat. Mater.*, 2013, **12**, 815–820.

14 H. Wang, L. L. Yu, Y. H. Lee, Y. M. Shi, A. Hsu, M. L. Chin, L. J. Li, M. Dubey, J. Kong and T. Palacios, *Nano Lett.*, 2012, **12**, 4674–4680.

15 B. W. H. Baugher, H. O. H. Churchill, Y. Yang and P. Jarillo-Herrero, *Nat. Nanotechnol.*, 2014, **9**, 262–267.

16 Y. J. Zhang, T. Oka, R. Suzuki, J. T. Ye and Y. Iwasa, *Science*, 2014, **344**, 725–728.

17 J. S. Ross, P. Klement, A. M. Jones, N. J. Ghimire, J. Yan, D. G. Mandrus, T. Taniguchi, K. Watanabe, K. Kitamura, W. Yao, D. H. Cobden and X. Xu, *Nat. Nanotechnol.*, 2014, **9**, 268–274.

18 A. Pospischil, M. M. Furchi and T. Mueller, *Nat. Nanotechnol.*, 2014, **9**, 257–261.

19 K. F. Mak, K. He, C. Lee, G. H. Lee, J. Hone, T. F. Heinz and J. Shan, *Nat. Mater.*, 2013, **12**, 207–211.

20 J. S. Ross, S. Wu, H. Yu, N. J. Ghimire, A. M. Jones, G. Aivazian, J. Yan, D. G. Mandrus, D. Xiao, W. Yao and X. Xu, *Nat. Commun.*, 2013, **4**, 1474.

21 A. Chernikov, T. C. Berkelbach, H. M. Hill, A. Rigosi, Y. L. Li, O. B. Aslan, D. R. Reichman, M. S. Hybertsen and T. F. Heinz, *Phys. Rev. Lett.*, 2014, **113**, 076802.

22 K. He, N. Kumar, L. Zhao, Z. Wang, K. F. Mak, H. Zhao and J. Shan, *Phys. Rev. Lett.*, 2014, **113**, 026803.

23 T. Korn, S. Heydrich, M. Hirmer, J. Schmutzler and C. Schueller, *Appl. Phys. Lett.*, 2011, **99**, 102109.

24 D. Lagarde, L. Bouet, X. Marie, C. R. Zhu, B. L. Liu, T. Amand, P. H. Tan and B. Urbaszek, *Phys. Rev. Lett.*, 2014, **112**, 047401.

25 L. Yuan and L. B. Huang, *Nanoscale*, 2015, **7**, 7402–7408.

26 M. Amani, P. Taheri, R. Addou, G. H. Ahn, D. Kiriya, D. H. Lien, J. W. Ager, R. M. Wallace and A. Jayey, *Nano Lett.*, 2016, **16**, 2786–2791.

27 C. J. Docherty, P. Parkinson, H. J. Joyce, M. H. Chiu, C. H. Chen, M. Y. Lee, L. J. Li, L. M. Herz and M. B. Johnston, *ACS Nano*, 2014, **8**, 11147–11153.

28 J. H. Strait, P. Nene and F. Rana, *Phys, Rev. B*, 2014, **90**, 245402.

29 X. F. Liu, H. Y. Yu, Q. Q. Ji, Z. H. Gao, S. F. Ge, J. Qiu, Z. F. Liu, Y. F. Zhang and D. Sun, *2D Mater.*, 2016, **3**, 014001.

30 E. M. Mannebach, K. A. Duerloo, L. A. Pellouchoud, M. J. Sher, S. Nah, Y. H. Kuo, Y. Yu, A. F. Marshall, L. Cao, E. J. Reed and A. M. Lindenberg, *ACS Nano*, 2014, **8**, 10734–10742.

31 C. Poellmann, P. Steinleitner, U. Leierseder, P. Nagler, G. Plechinger, M. Porer, R. Bratschitsch, C. Schuller, T. Korn

and R. Huber, *Nat. Mater.*, 2015, **14**, 889–893.

32 S. Cha, J. H. Sung, S. Sim, J. Park, H. Heo, M. H. Jo and H. Choi, *Nat. Commun.*, 2016, **7**, 10768.

33 A. G. Cabo, J. A. Miwa, S. S. Gronborg, J. M. Riley, J. C. Johannsen, C. Cacho, O. Alexander, R. T. Chapman, E. Springate, M. Grioni, J. V. Lauritsen, P. D. C. King, P. Hofmann and S. Ulstrup, *Nano Lett.*, 2015, **15**, 5883–5887.

34 Z. Nie, R. Long, L. Sun, C. C. Huang, J. Zhang, Q. Xiong, D. W. Hewak, Z. Shen, O. V. Prezhdo and Z. H. Loh, *ACS Nano*, 2014, **8**, 10931–10940.

35 F. Ceballos, Q. Cui, M. Z. Bellus and H. Zhao, *Nanoscale*, 2016, **8**, 11681–11688.

36 N. Kumar, Q. Cui, F. Ceballos, D. He, Y. Wang and H. Zhao, *Phys. Rev. B*, 2014, **89**, 125427.

37 D. Sun, Y. Rao, G. A. Reider, G. Chen, Y. You, L. Brezin, A. R. Harutyunyan and T. F. Heinz, *Nano Lett.*, 2014, **14**, 5625–5629.

38 B. A. Ruzicka, S. Wang, L. K. Werake, B. Weintrub, K. P. Loh and H. Zhao, *Phys. Rev. B*, 2010, **82**, 195414.

39 J. He, D. He, Y. Wang, Q. Cui, M. Z. Bellus, H.-Y. Chiu and H. Zhao, *ACS Nano*, 2015, **9**, 6436–6442.

40 R. Wang, B. A. Ruzicka, N. Kumar, M. Z. Bellus, H.-Y. Chiu and H. Zhao, *Phys. Rev. B*, 2012, **86**, 045406.

41 J. He, D. He, Y. Wang, Q. Cui, F. Ceballos and H. Zhao, *Nanoscale*, 2015, **7**, 9526.

42 N. Kumar, Q. Cui, F. Ceballos, D. He, Y. Wang and H. Zhao, *Nanoscale*, 2014, **6**, 4915–4919.

43 Q. Cui, F. Ceballos, N. Kumar and H. Zhao, *ACS Nano*, 2014, **8**, 2970–2976.

44 Q. Cui, J. He, M. Z. Bellus, M. Mirzokarimov, T. Hofmann, H.-Y. Chiu, M. Antonik, D. He, Y. Wang and H. Zhao, *Small*, 2015, **11**, 5565–5571.

45 Q. Cui, A. Lipatov, J. S. Wilt, M. Z. Bellus, X. C. Zeng, J. Wu, A. Sinitskii and H. Zhao, *ACS Appl. Mater. Interfaces*, 2016, **8**, 18334–18338.

46 H. Zhao, *Appl. Phys. Lett.*, 2008, **92**, 112104.

47 B. A. Ruzicka, L. K. Werake, H. Samassekou and H. Zhao, *Appl. Phys. Lett.*, 2010, **97**, 262119.

48 W. T. Hsu, Y. L. Chen, C. H. Chen, P. S. Liu, T. H. Hou, L. J. Li and W. H. Chang, *Nat. Commun.*, 2015, **6**, 8963.

49 Q. Wang, S. Ge, X. Li, J. Qiu, Y. Ji, J. Feng and D. Sun, *ACS Nano*, 2013, **7**, 11087–11093.

50 C. Mai, A. Barrette, Y. Yu, Y. G. Semenov, K. W. Kim, L. Cao and K. Gundogdu, *Nano Lett.*, 2013, **14**, 202–206.

51 S. Dal Conte, F. Bottegoni, E. A. A. Pogna, D. De Fazio, S. Ambrogio, I. Bargigia, C. D'Andrea, A. Lombardo, M. Bruna, F. Ciccacci, A. C. Ferrari, G. Cerullo and M. Finazzi, *Phys. Rev. B*, 2015, **92**, 235425.

52 N. Kumar, J. He, D. He, Y. Wang and H. Zhao, *Nanoscale*, 2014, **6**, 12690–12695.

53 C. Mai, Y. G. Semenov, A. Barrette, Y. F. Yu, Z. H. Jin, L. Y. Cao, K. W. Kim and K. Gundogdu, *Phys. Rev. B*, 2014, **90**, 041414.

54 C. R. Zhu, K. Zhang, M. Glazov, B. Urbaszek, T. Amand, Z. W. Ji, B. L. Liu and X. Marie, *Phys. Rev. B*, 2014, **90**, 161302.

55 L. Y. Yang, N. A. Sinitsyn, W. B. Chen, J. T. Yuan, J. Zhang, J. Lou and S. A. Crooker, *Nat. Phys.*, 2015, **11**, 830–834.

56 L. Y. Yang, W. B. Chen, K. M. McCreary, B. T. Jonker, J. Lou and S. A. Crooker, *Nano Lett.*, 2015, **15**, 8250–8254.

57 H. Shi, R. Yan, S. Bertolazzi, J. Brivio, B. Gao, A. Kis, D. Jena, H. G. Xing and L. Huang, *ACS Nano*, 2012, **7**, 1072–1080.

58 T. Yan, X. Qiao, X. Liu, P. Tan and X. Zhang, *Appl. Phys. Lett.*, 2014, **105**, 101901.

59 H. N. Wang, C. J. Zhang and F. Rana, *Nano Lett.*, 2015, **15**, 8204–8210.

60 M. Seo, H. Yamaguchi, A. D. Mohite, S. Boubanga-Tombet, J. C. Blancon, S. Najmaei, P. M. Ajayan, J. Lou, A. J. Taylor and R. P. Prasankumar, *Sci. Rep.*, 2016, **6**, 21601.

61 S. Schmitt-Rink, D. S. Chemla and D. A. B. Miller, *Phys. Rev. B*, 1985, **32**, 6601–6609.

62 F. Ceballos, P. Zereshki and H. Zhao, *Phys. Rev. Mater.*, 2017, **1**, 044001.

63 H.-L. Liu, C.-C. Shen, S.-H. Su, C.-L. Hsu, M.-Y. Li and L.-J. Li, *Appl. Phys. Lett.*, 2014, **105**, 201905.

64 F. Ceballos and H. Zhao, *Adv. Funct. Mater.*, 2017, **27**, 1604509.

65 A. Thilagam, *J. Appl. Phys.*, 2016, **120**, 124306.

66 P. Steinleitner, P. Merkl, P. Nagler, J. Mornhinweg, C. Schuller, T. Korn, A. Chernikov and R. Huber, *Nano Lett.*, 2017, **17**, 1455–1460.

67 C. Zhang, A. Johnson, C. L. Hsu, L. J. Li and C. K. Shih, *Nano Lett.*, 2014, **14**, 2443–2447.

68 H. M. Hill, A. F. Rigosi, C. Roquelet, A. Chernikov, T. C. Berkelbach, D. R. Reichman, M. S. Hybertsen, L. E. Brus and T. F. Heinz, *Nano Lett.*, 2015, **15**, 2992–2997.

69 Z. Ye, T. Cao, K. O'Brien, H. Zhu, X. Yin, Y. Wang, S. G. Louie and X. Zhang, *Nature*, 2014, **513**, 214–218.

70 M. M. Ugeda, A. J. Bradley, S. F. Shi, F. H. da Jornada, Y. Zhang, D. Y. Qiu, W. Ruan, S. K. Mo, Z. Hussain, Z. X. Shen, F. Wang, S. G. Louie and M. F. Crommie, *Nat. Mater.*, 2014, **13**, 1091–1095.

71 K. P. Wang, J. Wang, J. T. Fan, M. Lotya, A. O'Neill, D. Fox, Y. Y. Feng, X. Y. Zhang, B. X. Jiang, Q. Z. Zhao, H. Z. Zhang, J. N. Coleman, L. Zhang and W. J. Blau, *ACS Nano*, 2013, **7**, 9260–9267.

72 R. W. Boyd, *Nonlinear Optics*, Academy Press, San Diego, USA, 3rd edn, 2008.

73 N. Dong, Y. Li, Y. Feng, S. Zhang, X. Zhang, C. Chang, J. Fan, L. Zhang and J. Wang, *Sci. Rep.*, 2015, **5**, 14646.

74 S. Ge, X. Liu, X. Qiao, Q. Wang, Z. Xu, J. Qiu, P. H. Tan, J. Zhao and D. Sun, *Sci. Rep.*, 2014, **4**, 5722.
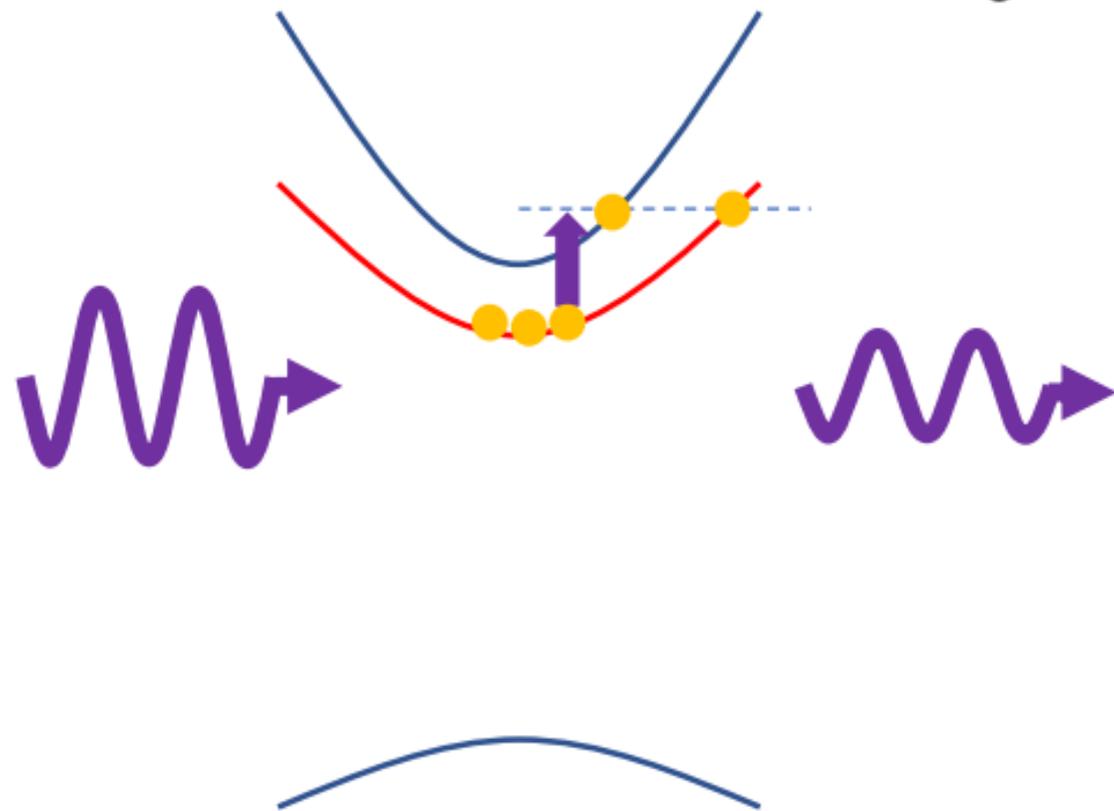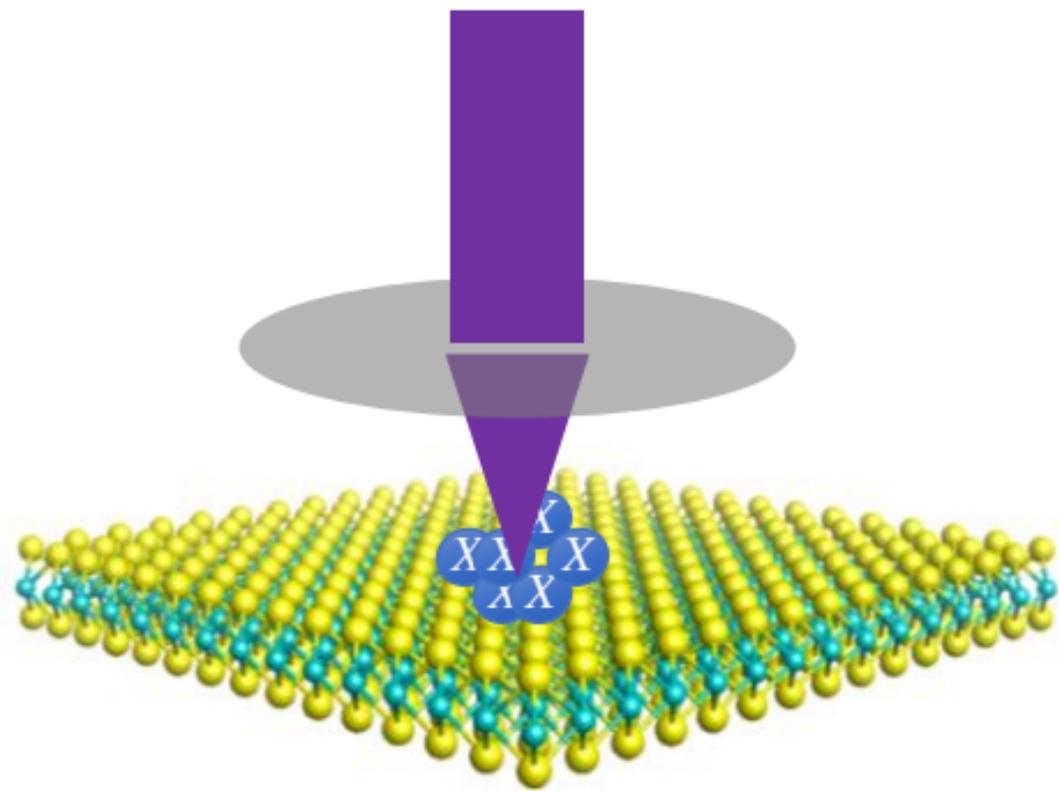
Excitonic intraband absorption is used to probe excitonic dynamics in monolayer transition metal dichalcogenides